ARTICLE

Received 00th January 20xx,

Accepted 00th January 20xx

DOI: 10.1039/x0xx00000x

Exploring Carbon Electrode Parameters in Li-O_2 Cells: Li_2O_2 and Li_2CO_3 Formation

Bianca P. Sousa[a], Chayene G. Anchieta[b], Thayane M. C. Nepel[a], Alex R. Neale[c], Laurence J. Hardwick[c], Rubens M. Filho[a], Gustavo Doubek[a]*

Ensuring the stability of the electrode and electrolyte in Li-O_2 batteries and achieving a comprehensive understanding of parasitic side reaction managment during cycling are key issues for the progress of this promising energy storage technology. Conditionsthat favour formation of either Li_2O_2 or Li_2CO_3 in Li-O_2 cells on carbon-based electodes were investigated. Operando Raman microscopy measurements and *ex situ* Raman and X-ray photoelectron spectroscopy (XPS) analyses were performed for Li-O_2 systems using Li[ClO_4]/DMSO as the electrolyte and carbon paper (CP) and carbon paper with carbon nanotubes (CPCNT) as electrodes. Using CP electrodes (either treated or untreated with O_2 plasma), the major discharge product formed was Li_2O_2. In contrast, for CPCNT electrodes, the formation of Li_2CO_3 as the main discharge product was observed at lower capacities, then significant formation of Li_2O_2 proceeded at higher discharge capacities. XPS highlighted that the surface chemistry of the CPCNT electrode comprised of fluorine and a variety of iron species, which could be linked to the promotion of Li_2CO_3 formation. Furthermore, it was observed that when Li_2CO_3 is the main discharge product, the active sites of functional groups on carbon surfaces that favour carbonate formation become coated/passivated. Consequently, the dominant reaction pathway then alters, leading to the growth of Li_2O_2 over the surface. These outcomes emphasized the important role in cycling stability of the active sites on carbon electrodes, arising from the synthesis process or possible contaminants.

Introduction

Lithium-oxygen (Li-O_2) batteries have attracted great interest due to their potential to provide a high specific energy density,[1–3] around 5 times higher than present Li-ion technologies.[4,5] Despite this, barriers including the understanding of reaction mechanisms and side reactions need to be clarified to achieve Li-O_2 batteries with long cycle lives and high capacities.[6]

In an ideal aprotic Li-O_2 cell during discharge, Li^+ combines with molecular O_2 to form lithium oxides (Li_2O_2, LiO_2) which are decomposed in a reversible process upon charging. [7,8] However, parasitic reactions can occur during these processes leading to low coulombic efficiency and rapid cell failure. The dominant side product lithium carbonate, Li_2CO_3, is an insulating species which is decomposed only at high potentials (>4.0 V).[9,10] Electrolyte oxidation and cathode decomposition reactions are possible sources of Li_2CO_3 in a Li-O_2 battery, both associated with cell deterioration. Carbonate-based electrolytes produce Li_2CO_3 as the primary discharge product due to their carbonyl groups being easily oxidized by superoxide species,[11–13] but several others studied electrolytes can also promote carbonate formation under certain conditions.[14–17]

With respect to the air cathode electrodes, carbon materials are attractive candidate materials due to their characteristics, such as low cost, low weight, and high conductivity.[18–21] Nonetheless, the highly reactive oxygen species present within discharge and charge processes can attack the carbon surface and induce the formation of carbonates and other organic species. McCloskey and colleagues attributed the carbonate formation from the reaction between Li_2O_2 and the carbon from the cathode surface.[22] On the other hand, Xu and co-workers verified that Li_2CO_3 was formed by electrolyte decomposition rather than from the carbon electrode during discharge.[23] This was confirmed by Thotiyl *et al*. who verified formation of Li_2CO_3 occurs at cell voltages above 3.5 V on the carbon cathode.[16] Recently, Itkins *et al*. proposed another route for Li_2CO_3 formation with superoxide attack to carbon (in activated double bonds) producing epoxy groups, followed by carbonate formation.[24] Although defects in carbon structure may favour Li_2CO_3 formation,[16,22,24] they have also been found to improve

[a] *Laboratory of Advanced Batteries, School of Chemical Engineering, University of Campinas (UNICAMP), 500, Avenida Albert Einstein, 13083-852, Campinas, São Paulo, Brazil.*
[b] *Swiss Light Source, Paul Scherrer Institut, Forschungsstrasse 111, 5232 Villigen, Switzerland.*
[c] *Stephenson Institute for Renewable Energy, Department of Chemistry, Peach Street, University of Liverpool, Liverpool L69 7ZF, United Kingdom.*
* Corresponding author. E-mail: doubek@unicamp.br
Electronic Supplementary Information (ESI) available: [details of any supplementary information available should be included here]. See DOI: 10.1039/x0xx00000x

the battery performance.[25–27] Some studies have shown the influence of defects[28–30] and dopants[31–33] on carbon matrix electrodes in both the discharge and charge processes. However, further experimental investigations are necessary to evaluate the air electrodes material design that favours the formation of products like Li_2CO_3, which is an important issue for Li-O_2 cell rechargeability.

In this work, operando and *ex situ* analyses were performed in different carbon cathodes in Li-O_2 batteries with Li[ClO_4]/dimethyl sulfoxide (DMSO) electrolyte. The aim was to improve understanding of the properties of the electrode materials that lead to distinct products formation during cell discharge. Operando Raman microscopy is a powerful technique for characterising the chemical products formed, as well as probing structural changes at the electrode, during the cycling process of a cell. It was observed that the main discharge products were distinct for the different carbon cathodes. Pristine or functionalised carbon paper cathodes produced Li_2O_2, whereas cathodes with carbon nanotubes, regardless of the manufacturer or binder used in the ink, produced Li_2CO_3. XPS analysis highlights that the surface chemistry is a crucial factor that contributes to the nature of lithium product formation.

Experimental

Electrodes preparation

Different types of air electrodes were prepared in this work, with all electrodes using carbon paper (CP) (Toray Carbon Paper, TGP-H-60) as the base: pure CP (without pre-treatment), CP with a carbon nanotube (CNT) ink, and functionalized CP. The CNTs used were either sourced from Sigma-Aldrich (SA) or CNT Co. Ltd (CCL). CNT inks were prepared with (25 mg) multi-walled CNT, binder (30 µL) Nafion (Sigma-Aldrich) or (6.4 mg) polytetrafluoroethylene (PTFE) (Sigma-Aldrich), and (1.25 mL) solvent mixture containing ultrapure water and isopropanol (4:3). The suspension and zirconia balls were mixed in a conditioning mixer (ARE-250 THINKY, Intertronics) for 10 minutes and dropped onto CP surface on both sides and left to dry in a fume hood for 24 h. The mass loading of the electrodes with CNT was approximately 0.8 mg cm^{-2}. The CP functionalisation was prepared using an oxygen plasma treatment, according to the Lobo and co-workers methodology,[34] with a plasma time of 2 and 4 minutes. To summarise, the electrodes and their respective abbreviations used for the experiments were: carbon paper without pre-treatment (CP); carbon paper with carbon nanotubes from Sigma Aldrich and Nafion binder (CPCNT_SA_Naf); carbon paper with carbon nanotubes from CNT Co. Ltd. and Nafion binder (CPCNT_CCL_Naf); Carbon paper with carbon nanotubes from Sigma Aldrich and PTFE binder (CPCNT_SA_PTFE). All the electrodes were dried at 100 °C in a vacuum oven for 30 minutes before being transferred to an Ar-filled glovebox (H_2O/O_2 <0.1 ppm) where they remained stored until be used.

Cell assembly and electrochemical operation

All Li-O_2 cells were assembled in the Ar-filled glovebox. The optical cell for operando measurements consists of an ECC-Opto-Std base (EL-Cell) and a custom-made stainless-steel lid with channels for O_2 flow and an aperture on the top for sapphire optical window (shown in Fig. S1 in supporting information). The lid was designed and 3D printed in-house. For deep discharge tests, the cell used was also developed in-house using Swagelok-type system for gas flow in one stainless steel plate, a second stainless steel plate, both with terminals for electrical contact, and a Teflon chamber between them (see Fig. S2 in supporting information). The cells for both tests were assembled in an analogous way, with a lithium metal foil electrode disk (Sigma-Aldrich) at the bottom, glass fibre separator (HNM-GF50/A) embedded with 100 µL of electrolyte 0.1 M Li[ClO_4] (Sigma-Aldrich) in anhydrous dimethyl sulfoxide (DMSO, Sigma-Aldrich). Then the specific carbon air electrode was placed on the top. The diameter of the battery components was distinct for each cell used, with electrodes measuring 9 mm in diameter for the EL-Cell/3D printed lid cell, and 16 mm for the Swagelok-type cell. To ensure complete wetting of the carbon cathode, the cells were rested in the glovebox for at least one day before electrochemical measurements. O_2 gas was purged into the cells at 1.5 barG and the system was sealed.

Electrochemical tests were conducted in a two-electrode cell configuration in galvanostatic mode with 65 µA cm^{-2} of applied current density. For operando tests, a Biologic SP-150e potentiostat was used to conduct discharge/charge cycles of 10 h per half-cycle test. Electrochemical deep discharge/charge tests were conducted using an Arbin potentiostat with a cell potential cut-off limit of 2.2 V and 4.5 V.

Raman spectroscopy

Raman spectroscopic analyses (Renishaw inVia) were conducted using a He-Ne 632.8 nm laser and a 50x objective. The measurement conditions were 60 s and 3 accumulations for operando testing, and 80 s and 5 accumulations for *ex situ* to improve the signal-to-noise ratios in the spectra. In operando tests, the spectra were collected every 1 h until the 20 h cycle was completed. For *ex situ* measurements, cells were submitted to 30 min of argon flow and the disassembled inside the glovebox after discharging. The electrodes were then sealed in a stainless-steel sample holder with a glass window.

X-ray photoelectron spectroscopy

XPS measurements were recorded using an Al Kα as X-ray source (Thermo Fisher Scientific X-ray photoelectron spectrometer). The analyses were performed under ultrahigh vacuum conditions. Ag and Au standard samples were used for calibration. The pristine CP and CP functionalized electrodes were investigated in a long scan and in C 1s, O 1s, and N 1s energies region. In addition to these regions, CPCNT electrodes were also analysed in the Fe and F energy region. XPS data were treated by subtracting Shirley-type background and employing Lorentzian/Gaussian functions for bands deconvolution.

Quantification of discharge product

Li_2O_2 mass was quantified by titration using Ti(IV)OSO_4 solution (Sigma-Aldrich, ~1.9–2.1 wt%) and an UV-vis spectrometer (Agilent, Cary 60). The titration with titanium oxysulfate solution is a well stablished procedure to determine the amount of Li_2O_2.[35,36] In this methodology, Li_2O_2 reacts with the H_2O of the solution forming LiOH and H_2O_2. In the presence of H_2O_2, a TiO_2SO_4 complex is formed, changing the solution from transparent to yellow/orange. A UV-Vis calibration curve was firstly determined by adding incremental mass of Li_2O_2 standard powder to the Ti(IV)OSO_4 solution and measuring absorbance at $\lambda = 406$ nm. The discharged electrodes were placed in a headspace vial and left to dry for 1 h at the glovebox after cell disassembly. After electrode drying the vial was sealed and taken from the glovebox and 4 mL of Ti(IV)SO_4 solution was added to the vial with a syringe. The resulting solution was then transferred to a quartz cuvette and analysed by UV-Vis spectroscopy.

Results and discussion

The operando Raman technique allows tracking of the reaction process in real time. Following the Raman bands during the discharge and charge processes of the Li-O_2 battery, it was possible to identify product formation and decomposition. In the present work, detailed analyses show that carbon-based electrodes with different structure and surface chemistry can alter the reaction pathways, producing different discharge products. Carbon paper (CP) leads to the formation of Li_2O_2 as the primary discharge product, while the addition of CNTs results in the formation of Li_2CO_3 as the main discharge product. Fig. 1 and Fig. 2 show the potential profiles and operando Raman spectra, respectively, of a pure CP electrode and a carbon paper with carbon nanotube (CPCNT) electrode using dimethyl sulfoxide (DMSO)/Li[ClO_4] as the electrolyte. Considering Fig. 1, the discharge potential profiles do not present significant differences for the different electrodes used, nevertheless the overpotential is higher for CP. Regarding the charging process, CP exhibits a different potential profile compared to the electrodes containing CNT, which will be discussed further in this work. In Fig.2, the Raman spectra are presented in 3D and 2D views between 700 to 1200 cm^{-1}, the primary range of interest for discharge products of Li-O_2 batteries. Electrolyte bands for DMSO (1040, 950 cm^{-1}) and Li[ClO_4] (935 cm^{-1}) are observed in all the spectra. In Table S1 of the Supporting Information (SI), all the bands of operando Raman spectra and their respective assignments are presented.

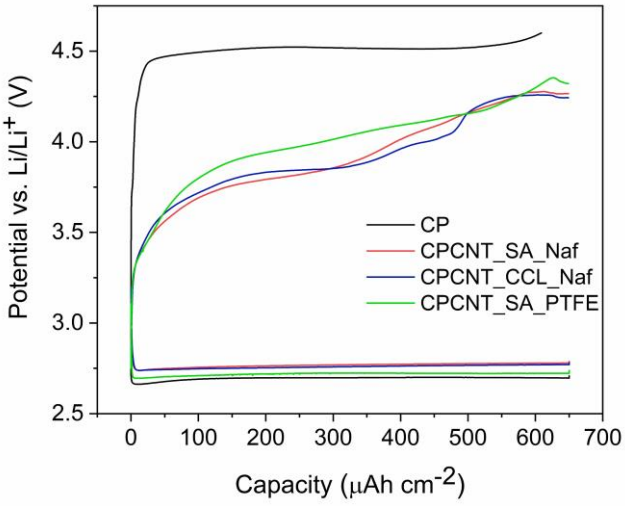

Fig. 1. Potential profiles of Carbon paper (CP), CP with CNT from Sigma Aldrich and Nafion (CPCNT_SA_Naf), CP with CNT from CNT Co. Ltd. and Nafion (CPCNT_CCL_Naf), and CP with CNT from Sigma Aldrich and PTFE (CPCNT_SA_PTFE) electrodes in Li-O_2 cells with 0.1 M Li[ClO_4] in DMSO electrolyte using a current density of 65 μA cm^{-2}.

Raman experiments conducted in a cell with a carbon paper as the air electrode (Fig. 2a) revealed the Li_2O_2 discharge product within 2 h from the start of discharge with a characteristic band at 790 cm^{-1} (O-O stretching) [7,37] with the intensity increasing during discharge. Li_2O_2 is the main expected product for an aprotic Li-O_2 battery and the mechanism proposed by most of studies involves an initial oxygen reduction (Equation 1), followed by Li^+ complexation (Equation 2) and lithium superoxide (LiO_2) disproportionation (Equation 3) to yield Li_2O_2. [6,20,38] Peng and co-workers highlighted LiO_2 intermediate formation using surface enhanced Raman spectroscopy (SERS) at a gold electrode in an acetonitrile-based electrolyte.[39] In our results, the characteristic superoxide band was not observed, probably because it remained in solution at low concentrations with a short lifetime. Additionally, there were no plasmonic nanoparticles employed in this work to enhance the Raman signal at the electrode interface. While some studies using DMSO have observed LiO_2 using SERS,[40–43] there are other studies using carbon paper electrode which also did not observe the superoxide feature by conventional (*i.e.,* non-surface enhanced) Raman spectroscopy.[44,45] In addition, Yu and Ye showed superoxide by UV-Vis spectroscopy, but no Raman bands pertaining to LiO_2 within a DMSO/Li[ClO_4] electrolyte, even with SERS.[46] The DMSO organic solvent has a high donor number (DN=29.8), [47] high basicity, and strong electron donating properties. The Li^+ acidity is softened on solvation by DMSO, so the soft base O_2^- has a strong affinity for the solvated cation, forming a DMSO-solvated LiO_2 in solution as the reaction intermediate.[48–50] Following the solution pathway mechanism, Li_2O_2 can be formed from LiO_2 disproportionation which generally grows as toroidal particles but can sometimes form a film on the electrode surface.[6,51,52]

$$O_2 + e^- \rightarrow O_2^- \quad (1)$$

$$O_2^- + Li^+ \rightarrow LiO_2 \quad (2)$$

$$2LiO_2 \rightarrow Li_2O_2 + O_2 \quad (3)$$

The Li_2O_2 band decreases during the charge process and completely disappears after 2 h. The oxygen evolution reaction (OER) mechanism that occurs upon charge, and the formation of reaction intermediates, remains an open question in the Li-O_2 batteries field.[2,6] A direct two-electron oxidation of Li_2O_2 using different electrolytes, including DMSO, is proposed by

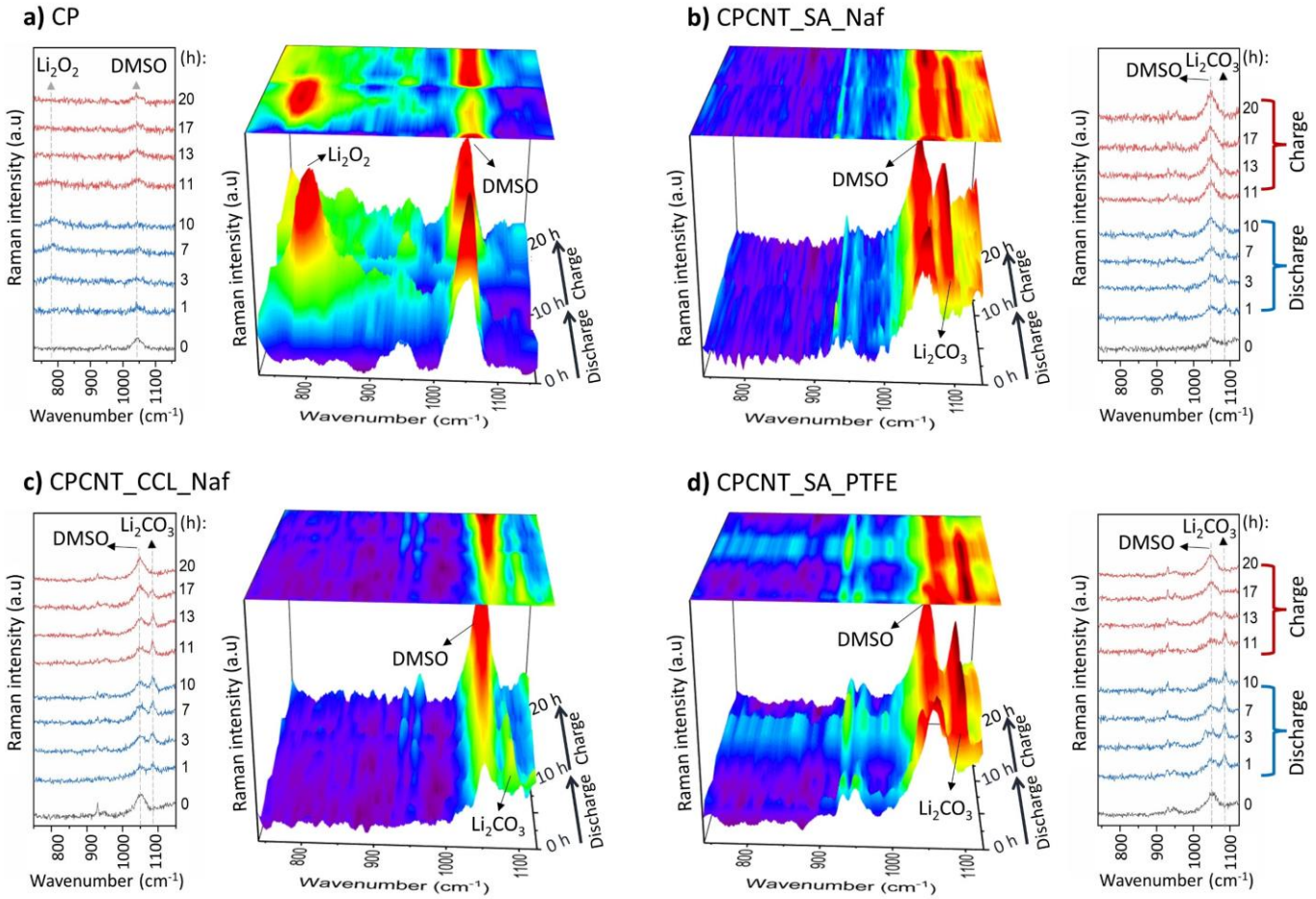

Fig. 2. Operando Raman spectra of Carbon paper (CP), CP with CNT from Sigma Aldrich and Nafion (CPCNT_SA_Naf), CP with CNT from CNT Co. Ltd. and Nafion (CPCNT_CCL_Naf), and CP with CNT from Sigma Aldrich and PTFE (CPCNT_SA_PTFE) electrodes in Li-O_2 cells with 0.1 M Li[ClO_4] in DMSO electrolyte using a current density of 65 µA cm^{-2}.

some authors based on cyclic voltammetry tests. [50,53,54] Peng and co-workers also noticed a direct decomposition of Li_2O_2 to O_2 formation on OER by *in situ* Raman spectroscopy and differential electrochemical mass spectrometry studies using acetonitrile as the electrolyte solvent. [39] Meanwhile, routes with more than one step for OER with $Li_{2-x}O_2$ and/or LiO_2 as the intermediate of Li_2O_2 decomposition are also reported in the literature. A lithium deficient phase $Li_{2-x}O_2$ formation and consequent O_2 release upon charging was proposed according to computational methods[55] and by *in situ* X-ray diffraction analysis with an electrolyte based on tetraglyme and (1 M) lithium bis{(trifluoromethyl)sulfonyl}imide.[56] Using rotating ring-disk electrode and X-ray absorption near edge tests, Wang and co-workers suggested Li_2O_2 oxidation occurs first by $Li_{2-x}O_2$ formation, then

O_2 release for low DN solvent or LiO_2 production before evolving O_2 in high DN solvent.[48] In addition, an initial delithiation of Li_2O_2, followed by LiO_2 formation then O_2 release was reported by Gallant *et al*. and Lu and Shao-Horn according to the steps upon charging. [57,58] Based on our results, we propose a two-electron oxidation reaction upon charging (Equation 4), without intermediate species formation.

$$Li_2O_2 \rightarrow O_2 + 2e^- + 2Li^+ \quad (4)$$

LiO_2 is unstable at potentials above 3.5 V and the electrochemical profile of CP/DMSO battery (Fig. 1) shows that the main discharge product, Li_2O_2, is decomposed in one step charge at 4.5 V. [6,39,58] This high charge overpotential for carbon paper was already noticed in literature due to the absence of a catalytic material for OER,[20,59,60] and the probable large particles size of Li_2O_2 formed during the discharge process.[2,61]

Electrolyte stability is an important factor to create long-life Li-O_2 batteries. Carbonates and ether-based solvents are known to decompose in Li-O_2 cells to form products like lithium carbonates, formates, and acetates. [12,14,62–64] Some studies have reported the oxidation of DMSO to dimethyl sulfone ($DMSO_2$), forming lithium carbonate and hydroxide,[16,38,65,66] while others report satisfactory DMSO stability with some specific cathodes.[11,67,68] In operando Raman of the CP/DMSO cell (Fig. 2a), no side products bands, such as lithium carbonate (Li_2CO_3 – 1090 cm^{-1}), dimethyl sulfone ($DMSO_2$ – 500, 1120 cm^{-1})[69] or lithium hydroxide (LiOH – 360, 630 cm^{-1})[7,70] were detected. The

absence of these bands indicates limited electrode and electrolyte decomposition with respect to scale detection. Moreover, the absence of LiOH and Li_2CO_3 also suggest no significant water and atmospheric air contaminants in the system.

In addition to the verified electrolyte stability, the charge overpotential is also an issue for cells since high overpotentials require more energy consumption. Thus, the introduction of active material to improve charging efficiencies is crucial for future applications. Cathodes with high surface areas like CNTs are of great interest for Li-O_2 batteries as they offer more reaction sites for ORR and OER and are good catalyst support materials.[8,71] Operando Raman spectra with elapsed time were collected to understand the product's evolution on CNTs and how the CNT addition alters the discharge chemistry (Fig. 2b, c & d). The use of CNT on CP electrodes (CPCNT) drastically changes the apparent reaction mechanism. In the Raman spectra of CPCNT electrodes, the Li_2CO_3 band at 1090 cm^{-1} emerges as early as 1 h into the discharge and remains present until 8 h of charging. Therein, no Li_2O_2 Raman band is detected for CPCNT electrodes during the discharge and charge processes of operando Raman tests. Comparing the results of the CNT-based electrode with the CP electrode (Fig. 2a), Li_2O_2 on CP is earlier decomposed than Li_2CO_3 on CPCNT. The decomposition of Li_2O_2 from the measured spectra was achieved after 2 h of charging while 9 h was required for Li_2CO_3.

It is well known that oxidation of the DMSO-based electrolyte is a potential source of Li_2CO_3 due to the high charging potentials or by the attack of superoxide species in discharge.[16,65,66,72] However, the data presented in Fig. 2 a-d shows that the main property responsible for the Li_2CO_3 formation in our experiments is the CNT, and the carbon source for the carbonate formation reaction can come either from the CNT itself or from the decomposition of DMSO that may be catalysed by the CNTs. This is supported since the cell with pure carbon paper (CNT-free electrode) showed no evidence of Li_2CO_3 formation and Li_2O_2 is the main discharge product.

Operando Raman microscopy measurements were also performed in cells using different carbon nanotubes and distinct binder materials (Fig. 2 b-d). Slight differences between the CNTs properties from Sigma Aldrich (CNT_SA) and from CNT Co. Ltd (CNT_CCL) can be noticed besides the manufacturer, such as carbon content, diameter, and length (Table S2 in supporting information). In addition, the XPS and Raman spectra (Fig. S3 a & b in supporting information, respectively) obtained from electrodes with the different types of CNTs show slight differences in the surface chemistry and defects. The electrode with CNT_SA presents a higher band of CF bond, a broader D Raman band and a higher I_D/I_G ratio. The I_D/I_G ratio is derived from the intensity ratio between the D and G band features and a larger ratio for the CNT_SA material indicates the presence of more structural defects compared to the CNT_CCL. Additionally, the binders used in the electrodes have different chemical compositions. PTFE is a fluoropolymer of tetrafluoroethylene, whereas Nafion (Naf) has a PTFE backbone and acidic sulfonic groups in its side chains. Despite these variations in CNTs and binders, the voltage profiles (Fig. 1) and associated Raman spectra obtained from Li-O_2 battery using CPCNT_SA_Naf (Fig. 2b), CPCNT_CCL_Naf (Fig. 2c), and CPCNT_SA_PTFE (Fig. 2d) as air electrodes show similar responses, with Li_2CO_3 identified as the main product. Lithium peroxide or other lithium oxides are not observed on any of these CNT-based electrodes at these discharge/charge capacities. The DMSO band in Fig. 2c appears to slightly increase, which may be attributed to microscope focusing issue/drift during the testing. These findings provide strong evidence that CNT plays a crucial role steering side reactions to form Li_2CO_3.

As shown in Fig. 1, the electrochemical profile of the cell with CPCNT_SA_Naf exhibits similar behaviour to the CPCNT_CCL_Naf and CPCNT_SA_PTFE but is distinct from CP. The cells with CPCNT electrodes showed one discharge plateau at 2.7 V, and two charge plateaus at *ca.* 3.8 V and 4.2 V. The second plateau is assigned to Li_2CO_3 decomposition, usually at 4.0-4.6 V as reported in the literature.[10,22,73] However, as the results revealed Li_2CO_3 as the main discharge product in CNT, the two-plateau behaviour upon charge must be further elucidated.

To address the reason for the first charge plateau in the battery with CPCNT electrodes, a deep investigation was carried out into the evolution of carbon bands in the Raman spectra. Fig. 3 a & b show the Raman spectra with elapsed time in the carbon region of CP and CPCNT_SA_Naf electrodes, respectively. The analogous operando Raman results of the other electrodes with CNT (CPCNT_CCL_Naf and CPCNT_SA_PTFE) are provided in Fig. S4. Carbon bands are featured at ~ 1330, 1580, 1615 cm^{-1} assigned to D, G and D' bands respectively. These bands correspond to well-known graphite bands, in which the G band appears due to the E_g Raman active phonons at Brillouin zone centre. The D and D' band are related to intervalley and intravalley, respectively, double resonance processes at the first Brillouin zone. The arising of D and D' bands require defects for its activation.[74] The ratio between the intensity of D and G bands gives information about defects in the carbonaceous structure, the higher I_D/I_G ratio means more defects in carbon. Fig. 3 c & d and Fig. S4 c & d in supporting information show the discharge/charge voltage profile with I_D/I_G ratio constructed by data collected from Raman bands spectra deconvolution for CP, CPCNT_SA_Naf, CPCNT_CCL_Naf, and CPCNT_SA_PTFE electrodes, respectively. The I_D/I_G ratio of CNTs increases upon charging, indicating the evolution of defects in the electrodes. These results coupled with the previous issue of the first plateau at ~3.8 V during the charge can be attributed to side reactions in the carbon surface. Carbonaceous materials with defects at the surface and functional groups in an oxidising medium with current applied can offer the necessary precursors for side reactions in the carbon surface of CNT.[24,75] The side reactions at the carbon surface are characteristic of CNTs, since no significant changes in the I_D/I_G ratio (and no evidence in the Raman spectra) are observed in carbon bands during the discharge/charge process using the CP electrode, indicating the stability of the carbon paper electrode as the air electrode for Li-O_2 batteries.

Moreover, to further elucidate the first charge plateau in the electrode with CNT, a titration analysis was performed on

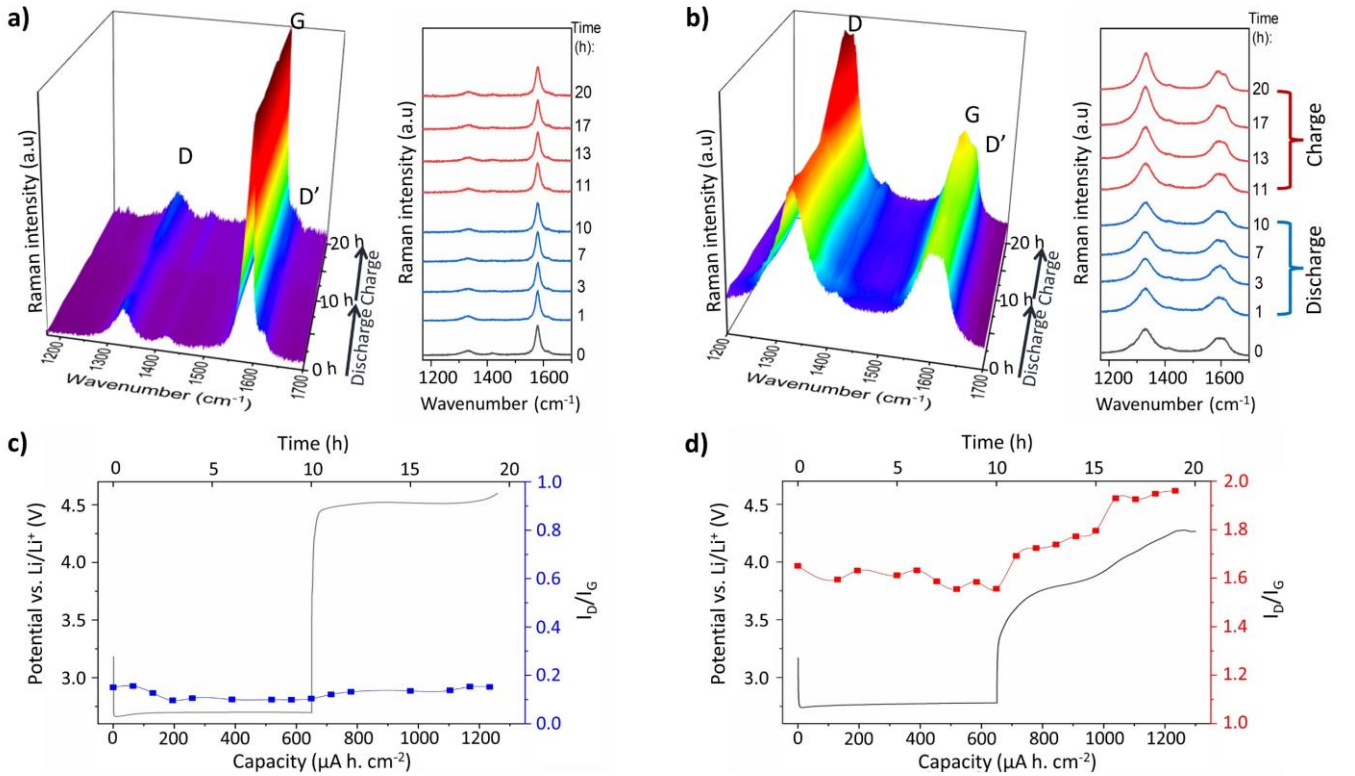

Fig. 3. Operando Raman spectra primary carbon bands during electrochemical discharge/charge at (a) carbon paper and (b) CP with CNT/Nafion electrodes. The corresponding voltage profiles are presented in (c) and (d), respectively, along with the derived I_D/I_G ratios. Both cells use a 0.1 M $LiClO_4$ in DMSO electrolyte with a current density of 65 μA cm^{-2}.

the CP and CPCNT_SA_Naf electrodes after a discharge of 650 μAh cm-² to evaluate the formation of Li_2O_2. The TiOSO4 solution after being in contact with the discharged CPCNT_SA_Naf had no significant change in the colour, maintaining a very light yellowish colour Conversely, the solution turned bright yellow when containing the discharged CP electrode (see Fig. S5 in supporting information). Using UV-Vis spectroscopy with the appropriate calibration, the mass of Li_2O_2 in discharged CP and

CPCNT_SA_Naf electrodes correspond to 82% and 2%, respectively, of the theoretical mass of Li_2O_2 formed in a perfect reaction for 650 μAh cm^{-2}. Assuming that the charge plateau observed at 3.8 V until *ca*. 325 μAh cm^{-2} for electrodes with CNT was a result of peroxide decomposition (as described by Equation 4), the theoretical mass expected of Li_2O_2 to be consumed at this charge capacity was calculated to be 0.18 mg. As the total amount of Li_2O_2 produced in discharge on the CPCNT_SA_Naf electrode was only 0.01 mg, it would correspond to 7% of the theoretical value (0.18 mg) for the 325 μAh cm^{-2} charge capacity. This analysis confirms that the 3.8 V plateau in the CPCNT_SA_Naf was mainly due to the oxidation of side reaction products and not from Li_2O_2.

Thus, based on the electrochemical cycling profile, the Li_2CO_3 detection as discharge product in the operando Raman spectra, the quantitative titration results, and the D band behaviour during the cycling process, it is demonstrated that carbonate was the main product formed for CNT-based electrodes. Minor Li_2O_2 formation follows the same explanation as indicated for the CP/DMSO (Equation 2 and 3). However, the exact mechanism for carbonate formation is not well established.

Itkins *et al.* proposed a pathway for Li_2CO_3 formation on discharge based on X-ray photoelectron spectroscopy experiments.[24] According to these authors, the superoxide radicals formed during discharge attacks double bonds or aromatics of carbon, activated by oxygenated groups and associated defects on carbon. The nucleophilic addition or electron transfer promoted by superoxide produces epoxy-groups formation on carbon, which are further converted to carbonate.

The Li_2CO_3 may also have been produced by the exothermic reaction between lithium peroxide and carbon.[8,20,76] Even though Li_2O_2 is not observed in operando Raman of CNTs electrodes (Fig. 2 b-d), it is detected in small amounts by chemical titration analysis of discharged CPCNT_SA_Naf electrode (see Fig. S5 in SI). So, Li_2O_2 must be present as small particles or thin film, below the detection limit of the Raman measurement. In addition, the small amount of Li_2O_2 formed during the operando test may react rapidly with carbon to form Li_2CO_3 on the surface, making it difficult for Li_2O_2 to accumulate to form detectable larger particles.

According to Itkins, carbonate formation could be favoured by defects and oxygenated functional groups in carbon structure.[24] Jiang and co-workers in a theoretical calculation for graphite indicate that specific types of defects: SV (single vacancy), DV5-8-5 (two pentagons and one octagon), and

DV555-777 (three pentagons and three heptagons) lead to Li_2CO_3 formation.[28] In order to obtain an imporved understanding of how defects can influence the Li_2CO_3 evolution, an oxygen plasma functionalisation of the pure carbon paper was conducted. The procedure successfully introduced defects onto the CP surface (denoted "CP-functionalised") as could be verified by the significant increase in the intentisty of D band (Fig. S6 a in supporting information) compared with the pristine material. Also, D* and D" bands related to functional groups and amorphous carbon, respectively,[77–79] appear in the CP-functionalised in comparison with the pristine CP.[77–79] XPS spectra of CP and CP-functionalised are shown in Fig. S6 b in supporting information, indicating a significant increase in the bands related to C-O and C=O bonds in the CP functionalised as compared to CP. Operando electrochemical Raman microscopy measurement with CP-functionalised revealed the similar behaviour to pristine CP, where only the Li_2O_2 was produced as discharge product (Fig. S7 in supporting information). Therefore, even in the functionalised CP containing defects and oxygen functional groups, no Li_2CO_3 band was observed. Eckman and co-workers[80] highlighted that the nature of defect in carbon structure (in this case graphene) can be determined by the ratio between the intensities of D and D' Raman bands. Values of $I_D/I_{D'}$ ~ 13, 7 and 3.5 were attributed for sp^3, vacancy and boundary types, respectively Furthermore, Jiang et al. determined $I_D/I_{D'}$ ratios for more specific and common defects in carbon, as Stone-Wales, single and di vacancies by calculations in graphene.[81] Here, for pristine CP, the $I_D/I_{D'}$ is 0.8 (see Fig. S6 in supporting information) indicating single vacancies defect type. In contrast, CP-functionalised (Fig. S6 in supporting information) present an $I_D/I_{D'}$ ratio of ~2.7, indicating DV 555-777 defect type, approximately the same D bands ratio that CPCNT_SA and CPCNT_CCL (Fig. S3b in supporting information). Thus, considering that the CP with CNTs and CP functionalised are likely to have similar types of defects, it can be concluded that the nature of defects is not the primary reason for the formation of carbonates in carbon electrodes.

Instead of only defects, the chemical composition of the surface that appears to explain the preferential formation of carbonates. To investigate this further, the electrode surfaces were characterised by XPS analysis. XPS revealed the presence of fluorine and iron in the CPCNT electrode, in addition to carbon and oxygen present in both CP and CP functionalised (see Fig. 4 a). The fluorine peak appears due to the binder used in CNT ink, since Nafion and PTFE are fluoropolymers. The presence of iron in the CNT arises from the manufacturing process, where nanoparticulate iron is used as a catalyst during the CNT production.[82,83] In this CNT growth process, carbon binds to iron, forming iron carbide (Fe_3C) as a stable intermediate.[84,85] By comparing the XPS spectra of the CPCNT electrode before and after the discharge, it is possible to

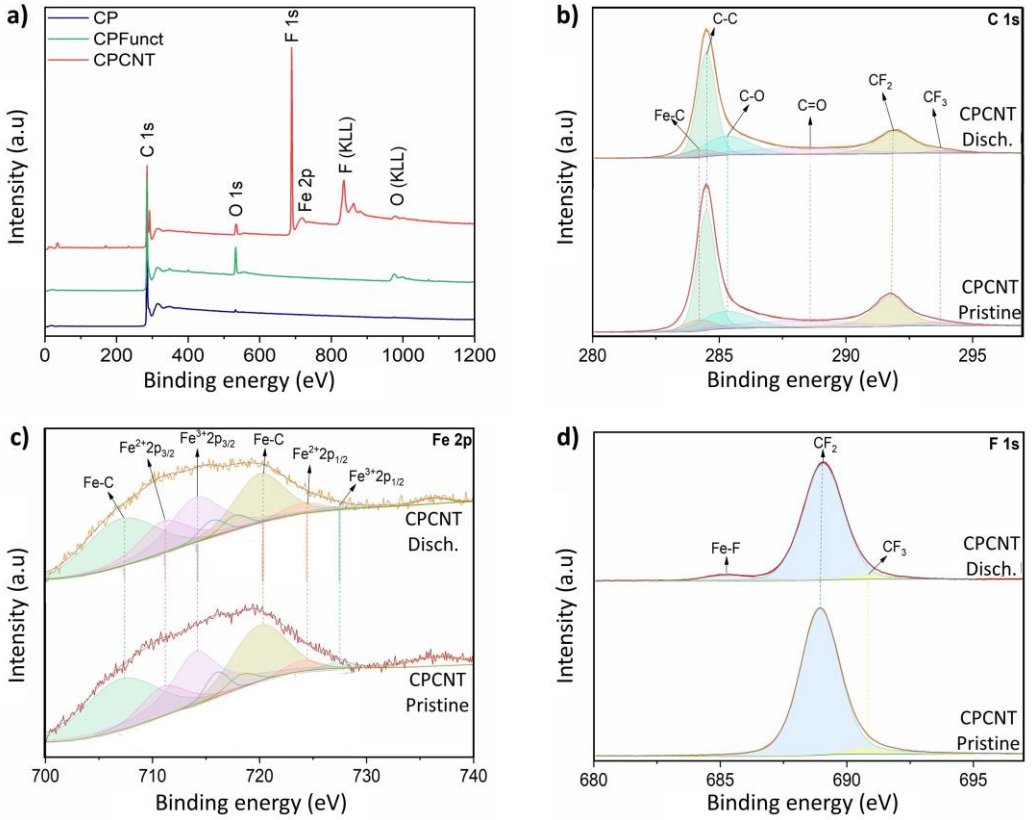

Fig. 4. XPS survey scan spectra of carbon paper (CP), CP functionalized, and CP with CNT (a). XPS spectra C1s (b), Fe2p (c), and F1s (d) XPS spectra for CPCNT pristine and discharged sample.

identify changes in the iron, carbon, and fluorine peaks, indicating that these species are modified with the occurrence of reactions during discharge.

Fig. 4b, c and d present the XPS spectra of CPCNT electrode in the C 1s, Fe 2p and F 1s energy, respectively, and Table S3 in supporting information their corresponding peaks assignments. C 1s spectra is deconvoluted into six peaks, which are attributed to the bonds Fe-C (284.1 eV),[86] C-C (284.5 eV), C-O (285.3 eV),[87] C=O (288.0 eV), CF_2 (291.9 eV), and CF_3 (293.8 eV),[88] pointing out that carbon is directly binding with iron, oxygen and fluorine in the CPCNT electrode. Fe-C bond is also observed in Fe 2p spectra at 707.0 and 720.0 eV, confirming the presence of iron carbide in the material.[89,90] In addition, XPS in Fe 2p energy contains peaks at 711.0, and 724.0 eV assigned to $Fe2p_{3/2}$ and $Fe2p_{1/2}$ of Fe^{2+}; and at 714.0 and 727.0 eV attributed to $Fe2p_{3/2}$ and $Fe2p_{1/2}$ of Fe^{3+}.[91–93] The presence of Fe^{2+} and Fe^{3+} ions indicate the existence of iron oxides species in the CPCNT electrode. In accordance with these observations in XPS analyses, the literature reports ^{57}Fe Mössbauer spectra of carbon nanotubes, in which Fe_3C is the main specie present, in addition to FeO and α-Fe species also noticed.[94–96]

The percentage areas of the XPS spectra of CPCNT pristine and discharged are presented in Table S3 in supporting information. After discharge, Fe-C and F-C bonds decrease, while a Fe-F bonding arises. In addition, more discretely, Fe^{2+} increase and Fe^{3+} decrease. According to Jiang, the O-O bond breakage is the main requirement for carbonate formation.[28] It is also well known that Fe^{2+} [97–100] and F [101–103] may act as a catalyst for the oxygen reduction reaction and breaking of the O_2 bond. Thus, unlike the CP electrode, in CP with CNT and binder, the presence of iron and fluorine, combined with defects in the material, could contribute to the Li_2CO_3 formation process.[3,82,86]

In the XPS spectra, in the C 1s energy of pristine and discharged CP electrodes, no significant difference is observed in the peaks, but only a slight change in the C-C and C-O bonds, probably due to the presence of Li_2O_2 in discharged electrode (shown in Fig. S8 in SI).

It has been reported that the electrochemical potential for oxygen reduction and, consequently, the reaction products formed are directly influenced by the activity of functional groups on carbon electrodes.[91,104,105] Considering this, the presence of Fe and F in the CPCNT electrodes should influence in the cell voltage and thus promote the formation of lithium carbonate during the discharge.

Cells with DMSO/Li[ClO_4] electrolyte and CP and CPCNT electrodes were also submitted to a full discharge test with a cut-off potential of 2.2 V to verify the products formed at larger discharge capacities, then to a full discharge/charge test (Fig. 5 a). Overall, the cell with CPCNT electrodes exhibit an electrochemical profile with a lower overpotential and delivering a higher capacity than the CP cell. The discharge potential plateau was at 2.78 V and 2.72 V for the cells based on CPCNT and CP, respectively. Regarding the charge curves, the voltage plateau was at ~ 4.43 V and 4.30 V for the cell with CPCNT and CP electrodes, respectively. The cell capacity with CPCNT electrode (2.61 mAh cm^{-2}) was about 2x higher than the cell with CP (1.25 mAh cm^{-2}). Due to the enhanced surface area and many additional sites introduced for ORR and OER, CNTs have been shown to deliver improved electrochemical performance.[21,106,107]

Subsequent to the discharge step, the CP and CPCNT electrodes were analysed by *ex situ* Raman microscopy. Fig. 5 b shows the *ex situ* Raman spectra of CP and CPCNT. In the deep discharged CP electrode, only the Li_2O_2 band was observed at 790 cm^{-1} in addition to the DMSO, Li[ClO_4] and carbon features. Exclusive Li_2O_2 formation in the CP electrode discharged until 2.2 V is in accordance with the operando measurements (Fig. 2 a) with a ~2x lower capacity of one cycle. On the other hand, in the CPCNT electrode Raman spectrum, besides the Li_2CO_3 band that was consistently observed in operando measurements (Fig. 2 b), the Li_2O_2 band feature was also observed. Despite the nonappearance in the operando Raman spectra, Li_2O_2 was formed in the CPCNT cell discharged until 0.65 mAh cm^{-2} in small amount as confirmed by titration analyse (Fig. S5 in supporting information). However, with 4x higher capacity than the

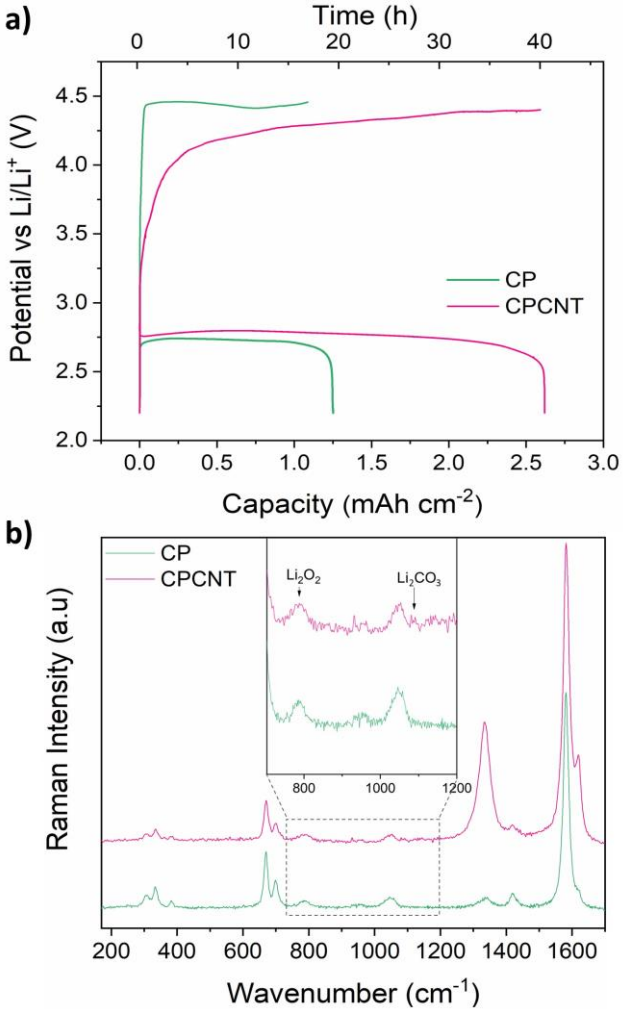

Fig. 5. (a) Deep discharge/charge potential profiles and (b) *ex situ* Raman spectra of carbon paper (CP) and CP with CNT electrodes. Both cells used 0.1 M Li[ClO_4] in DMSO electrolyte with a current density of 65 µA cm^{-2}.

operando measurements, the specific defects and active sites for Li_2CO_3 formation were likely coated/passivated and the other "regular" sites afforded the formation and growth of Li_2O_2 particles. Gallant and co-workers noticed by XANES major formation of Li_2CO_3 and Li_2O_2 at lower and higher capacities, respectively, for CNT electrode also. [63]

These operando Raman, *ex situ* Raman, and XPS results for CPCNT cathode with DMSO/Li[ClO_4] electrolyte contribute to a more detailed understanding of the influence of lithium products formation using different carbon materials for air electrodes in Li-O_2 cells. Upon discharge on carbon paper with CNT electrodes, there is an initial formation of Li_2CO_3 at smaller capacities (0.65 mAh cm^{-2}). At later stages, when fewer non-carbon sites are available, Li_2O_2 can nucleate at higher capacity (2.61 mAh cm^{-2}). During the charge, in addition to discharge product decomposition, side reactions at the carbon surface occur in the CNT cathode due to the oxidising environment with applied current, causing structural defects on carbon cathode. These results bring insights to the suitable choice of carbon cathode materials for use in in Li-O_2 batteries. While CNT has favourable characteristics of large surface area that can promote higher capacities, the structural defects and surface chemistry of CNT and binder can lead to the formation of unwanted Li_2CO_3 before the desired Li_2O_2. These outcomes further highlight the necessary requirement of redox mediators in Li-O_2 cells to move product formation/decomposition away from the electrode surface.

Conclusions

In this study, the impact of materials design on the air electrodes of the Li-O_2 battery and their roles in the formation pathways of discharge products were investigated. Raman measurements were conducted in an operando Li-O_2 cell using Li[ClO_4]/DMSO as electrolyte and carbon paper (CP) electrodes, both with and without carbon nanotubes (CNT). In the case of CP electrodes combined with CNT (CPCNT), the analysis revealed Li_2CO_3 as the main discharge product observed, regardless of the CNT supplier or the binder material used. Conversely, using a CP electrode led to Li_2O_2 formation instead of Li_2CO_3, even when the same vacancy defects as CPCNT were artificially introduced in the CP electrode. Therefore, it was demonstrated that not only functional groups played a pivotal role in determining the nature of the discharge products, but also the surface chemistry of CNTs as shown by XPS analysis. It was observed that fluorine and iron species within the CNT and electrode could contribute to the observed carbonate formation. Moreover, after a deep discharge of 45 h using the CPCNT electrode, Li_2O_2 was detected in addition to Li_2CO_3. This indicates that Li_2CO_3 is the main product formed in the early stages of discharge but is subsequently further coated by Li_2O_2, probably due to the lower number of active sites available. In conclusion, material selection for the electrode is of significant importance for Li-O_2 batteries due to their potential to profoundly influence the formation of the discharge product.

Author Contributions

BPS: conceptualization, methodology, investigation, formal analysis, data curation; CAG: conceptualization, formal analysis, data curation; TCMN: formal analysis, validation, data curation; ARN: formal analysis, validation, data curation; LH: supervision, validation, resources; RMF: supervision, funding acquisition; GD: conceptualization, validation, supervision, funding acquisition. BPS, CAG and TCMP: writing original draft, review and editing; ARN, LH, RMF, and GD: review and editing the manuscript.

Conflicts of interest

There are no conflicts to declare.

Acknowledgements

Authors would like to thank Bruno A. B. Francisco and Julia P. de O. Julio their support with electrochemical measurements. This research supported by LNNano – Brazilian Nanotechnology National Laboratory (CNPEM/MCTI) during the use of the X-ray photoemission spectroscopy open access facility. This work was supported by the São Paulo Research Foundation (FAPESP) grant 2017/11958-1, the Unicamp Development Foundation (Funcamp) grant 5333.8, the Conselho Nacional de Desenvolvimento Científico e Tecnológico (CNPq) grant 201106/2020-5, the Coordenação de Aperfeiçoamento de Pessoal de Nível Superior – Brasil (CAPES), and Shell and the strategic importance of the support given by ANP (Brazil's National Oil, Natural Gas and Biofuels Agency) through the R&D levy regulation. ARN and LJH acknowledge the UK Faraday Institution (EPSRC EP/S003053/1) through the Degradation Project (grant numbers FIRG001 and FIRG024).

References

1. Girishkumar, G., McCloskey, B., Luntz, A. C., Swanson, S. & Wilcke, W. Lithium-air battery: Promise and challenges. *Journal of Physical Chemistry Letters* **1**, 2193–2203 (2010).

2. Shu, C., Wang, J., Long, J., Liu, H. K. & Dou, S. X. Understanding the Reaction Chemistry during Charging in Aprotic Lithium–Oxygen Batteries: Existing Problems and Solutions. *Advanced Materials* vol. 31 Preprint at https://doi.org/10.1002/adma.201804587 (2019).

3. Liu, K. *et al.* Insights into the activity of single-atom Fe-N-C catalysts for oxygen reduction reaction. *Nat Commun* **13**, (2022).

4. Fichtner, M. *et al.* Rechargeable Batteries of the Future—The State of the Art from a BATTERY 2030+ Perspective. *Advanced Energy Materials* vol. 12 Preprint at https://doi.org/10.1002/aenm.202102904 (2022).

5. Cremasco, L. F. *et al.* Operando Synchrotron XRD of Bromide Mediated Li-O2Battery. *ACS Appl Mater Interfaces* **13**, 13123–13131 (2021).

6. Wang, Y. & Lu, Y. C. Nonaqueous Lithium–Oxygen batteries: Reaction mechanism and critical open questions. *Energy Storage Materials* vol. 28 235–246 Preprint at https://doi.org/10.1016/j.ensm.2020.03.007 (2020).

7. Gittleson, F. S. *et al.* Raman Spectroscopy in Lithium-Oxygen Battery Systems. *ChemEletroChem* 1446–1457 (2015).

8. Tan, P. *et al.* Advances and challenges in lithium-air batteries. *Applied Energy* vol. 204 780–806 Preprint at https://doi.org/10.1016/j.apenergy.2017.07.054 (2017).

9. Ling, C. & Mizuno, F. Capture Lithium in αMnO2: Insights from First Principles. *Chem. Mater.* **24**, 3943 (2012).

10. Qiao, Y. *et al.* Li-CO2 Electrochemistry: A New Strategy for CO2 Fixation and Energy Storage. *Joule* **1**, 359–370 (2017).

11. Peng, Z., Freunberger, S. A., Chen, Y. & Bruce, P. G. A Reversible and Higher-Rate Li-O 2 Battery. *Science (1979)* (2012).

12. McCloskey, B. D., Bethune, D. S., Shelby, R. M., Girishkumar, G. & Luntz, A. C. Solvents critical role in nonaqueous Lithium-Oxygen battery electrochemistry. *Journal of Physical Chemistry Letters* **2**, 1161–1166 (2011).

13. Balaish, M., Kraytsberg, A. & Ein-Eli, Y. A critical review on lithium-air battery electrolytes. *Physical Chemistry Chemical Physics* vol. 16 2801–2822 Preprint at https://doi.org/10.1039/c3cp54165g (2014).

14. Freunberger, S. A. *et al.* The lithium-oxygen battery with ether-based electrolytes. *Angewandte Chemie - International Edition* **50**, 8609–8613 (2011).

15. Zhou, B. *et al.* A High-Performance Li–O2 Battery with a Strongly Solvating Hexamethylphosphoramide Electrolyte and a LiPON-Protected Lithium Anode. *Advanced Materials* **29**, (2017).

16. Ottakam Thotiyl, M. M., Freunberger, S. A., Peng, Z. & Bruce, P. G. The carbon electrode in nonaqueous Li-O2 cells. *J Am Chem Soc* **135**, 494–500 (2013).

17. Zhao, Z., Huang, J. & Peng, Z. Achilles' Heel of Lithium–Air Batteries: Lithium Carbonate. *Angewandte Chemie - International Edition* vol. 57 3874–3886 Preprint at https://doi.org/10.1002/anie.201710156 (2018).

18. Liu, Q. C. *et al.* A Flexible and Wearable Lithium–Oxygen Battery with Record Energy Density achieved by the Interlaced Architecture inspired by Bamboo Slips. *Advanced Materials* **28**, 8413–8418 (2016).

19. Sun, B., Huang, X., Chen, S., Munroe, P. & Wang, G. Porous graphene nanoarchitectures: An efficient catalyst for low charge-overpotential, long life, and high capacity lithium-oxygen batteries. *Nano Lett* **14**, 3145–3152 (2014).

20. Zhang, P. *et al.* Challenges and Strategy on Parasitic Reaction for High-Performance Nonaqueous Lithium–Oxygen Batteries. *Advanced Energy Materials* vol. 10 Preprint at https://doi.org/10.1002/aenm.202001789 (2020).

21. Ma, Z. *et al.* A review of cathode materials and structures for rechargeable lithium-air batteries. *Energy and Environmental Science* vol. 8 2144–2198 Preprint at https://doi.org/10.1039/c5ee00838g (2015).

22. McCloskey, B. D. *et al.* Twin problems of interfacial carbonate formation in nonaqueous Li-O 2 batteries. *Journal of Physical Chemistry Letters* **3**, 997–1001 (2012).

23. Xu, W. *et al.* The stability of organic solvents and carbon electrode in nonaqueous Li-O 2 batteries. *J Power Sources* **215**, 240–247 (2012).

24. Itkis, D. M. *et al.* Reactivity of carbon in lithium-oxygen battery positive electrodes. *Nano Lett* **13**, 4697–4701 (2013).

25. Yu, W. *et al.* Edge-Site-Free and Topological-Defect-Rich Carbon Cathode for High-Performance Lithium-Oxygen Batteries. *Advanced Science* (2023) doi:10.1002/advs.202300268.

26. Nakanishi, S., Mizuno, F., Nobuhara, K., Abe, T. & Iba, H. Influence of the carbon surface on cathode deposits in non-aqueous Li-O 2 batteries. *Carbon N Y* **50**, 4794–4803 (2012).

27. Huang, S., Fan, W., Guo, X., Meng, F. & Liu, X. Positive role of surface defects on carbon nanotube cathodes in overpotential and capacity retention of rechargeable lithium-oxygen batteries. *ACS Appl Mater Interfaces* **6**, 21567–21575 (2014).

28. Jiang, H. R., Tan, P., Liu, M., Zeng, Y. K. & Zhao, T. S. Unraveling the Positive Roles of Point Defects on Carbon Surfaces in Nonaqueous Lithium-Oxygen Batteries. *Journal of Physical Chemistry C* **120**, 18394–18402 (2016).

29. Belova, A. I., Kwabi, D. G., Yashina, L. V., Shao-Horn, Y. & Itkis, D. M. Mechanism of oxygen reduction in aprotic Li-air batteries: The role of carbon electrode surface structure. *Journal of Physical Chemistry C* **121**, 1569–1577 (2017).

30. Carvalho, V. S. *et al.* Radially ordered carbon nanotubes performance for Li-O2 batteries: Pre-treatment influence on capacity and discharge products. *Catal Today* **348**, 299–306 (2020).

31. Ren, X. *et al.* The doping effect on the catalytic activity of graphene for oxygen evolution reaction in a lithium-air battery: A first-principles study. *Physical Chemistry Chemical Physics* **17**, 14605–14612 (2015).

32. Jiang, H. R., Zhao, T. S., Shi, L., Tan, P. & An, L. First-Principles Study of Nitrogen-, Boron-Doped Graphene and Co-Doped Graphene as the Potential Catalysts in Nonaqueous Li–O2 Batteries. *The Journal of Physical Chemistry C* **120**, 6612–6618 (2016).

33. Huang, H. *et al.* Surface Phosphatization for a Sawdust-Derived Carbon Catalyst as Kinetics Promoter and Corrosion Preventer in Lithium–Oxygen Batteries. *Adv Funct Mater* **32**, (2022).

34. Lobo, A. O. *et al.* Fast functionalization of vertically aligned multiwalled carbon nanotubes using oxygen plasma. *Mater Lett* **70**, 89–93 (2012).

35. Wang, H. H. *et al.* Lithium Superoxide Hydrolysis and Relevance to Li-O2 Batteries. *Journal of Physical Chemistry C* **121**, 9657–9661 (2017).

36. Plunkett, S. T. *et al.* Charge Transport Properties of Lithium Superoxide in Li-O2Batteries. *ACS Appl Energy Mater* **3**, 12575–12583 (2020).

37. Neale, A. R. *et al.* Design Parameters for Ionic Liquid–Molecular Solvent Blend Electrolytes to Enable Stable Li Metal Cycling Within Li–O2 Batteries. *Adv Funct Mater* **31**, (2021).

38. Nepel, T. C. M. *et al.* In Situ Infrared Micro and Nanospectroscopy for Discharge Chemical

Composition Investigation of Non-Aqueous Lithium–Air Cells. *Adv Energy Mater* **11**, (2021).

39. Peng, Z. *et al.* Oxygen reactions in a non-aqueous Li+ electrolyte. *Angewandte Chemie - International Edition* **50**, 6351–6355 (2011).

40. Johnson, L. *et al.* The role of LiO 2 solubility in O 2 reduction in aprotic solvents and its consequences for Li-O 2 batteries. *Nat Chem* **6**, 1091–1099 (2014).

41. Gittleson, F. S., Ryu, W. H. & Taylor, A. D. Operando observation of the gold-electrolyte interface in Li-O2 batteries. *ACS Appl Mater Interfaces* **6**, 19017–19025 (2014).

42. Galloway, T. A. & Hardwick, L. J. Utilizing in Situ Electrochemical SHINERS for Oxygen Reduction Reaction Studies in Aprotic Electrolytes. *Journal of Physical Chemistry Letters* **7**, 2119–2124 (2016).

43. Galloway, T. A., Cabo-Fernandez, L., Aldous, I. M., Braga, F. & Hardwick, L. J. Shell isolated nanoparticles for enhanced Raman spectroscopy studies in lithium-oxygen cells. *Faraday Discuss* **205**, 469–490 (2017).

44. Dilimon, V. S., Lee, D. G., Yim, S. D. & Song, H. K. Multiple roles of superoxide on oxygen reduction reaction in Li+-containing nonaqueous electrolyte: Contribution to the formation of oxide as well as peroxide. *Journal of Physical Chemistry C* **119**, 3472–3480 (2015).

45. Gunasekara, I., Mukerjee, S., Plichta, E. J., Hendrickson, M. A. & Abraham, K. M. Microelectrode Diagnostics of Lithium-Air Batteries. *J Electrochem Soc* **161**, A381–A392 (2014).

46. Yu, Q. & Ye, S. In Situ Study of Oxygen Reduction in Dimethyl Sulfoxide (DMSO) Solution: A Fundamental Study for Development of the Lithium-Oxygen Battery. *Journal of Physical Chemistry C* **119**, 12236–12250 (2015).

47. Aetukuri, N. B. *et al.* Solvating additives drive solution-mediated electrochemistry and enhance toroid growth in non-aqueous Li-O2 batteries. *Nat Chem* **7**, 50–56 (2015).

48. Wang, Y. *et al.* A Solvent-Controlled Oxidation Mechanism of Li2O2 in Lithium-Oxygen Batteries. *Joule* **2**, 2364–2380 (2018).

49. Abraham, K. M. Electrolyte-Directed Reactions of the Oxygen Electrode in Lithium-Air Batteries. *J Electrochem Soc* **162**, A3021–A3031 (2015).

50. Trahan, M. J., Mukerjee, S., Plichta, E. J., Hendrickson, M. A. & Abraham, K. M. Studies of Li-Air Cells Utilizing Dimethyl Sulfoxide-Based Electrolyte. *J Electrochem Soc* **160**, A259–A267 (2013).

51. Aurbach, D., McCloskey, B. D., Nazar, L. F. & Bruce, P. G. Advances in understanding mechanisms underpinning lithium-air batteries. *Nature Energy* vol. 1 Preprint at https://doi.org/10.1038/nenergy.2016.128 (2016).

52. Galloway, T. A., Attard, G. & Hardwick, L. J. An electrochemical investigation of oxygen adsorption on Pt single crystal electrodes in a non-aqueous Li+ electrolyte. *Electrochem commun* **119**, 106814 (2020).

53. Laoire, C. O., Mukerjee, S., Abraham, K. M., Plichta, E. J. & Hendrickson, M. A. Elucidating the mechanism of oxygen reduction for lithium-air battery applications. *Journal of Physical Chemistry C* **113**, 20127–20134 (2009).

54. Laoire, C. O., Mukerjee, S., Abraham, K. M., Plichta, E. J. & Hendrickson, M. A. Influence of nonaqueous solvents on the electrochemistry of oxygen in the rechargeable lithium-air battery. *Journal of Physical Chemistry C* **114**, 9178–9186 (2010).

55. Kang, S., Mo, Y., Ong, S. P. & Ceder, G. A facile mechanism for recharging Li2O2 in Li-O 2

batteries. *Chemistry of Materials* **25**, 3328–3336 (2013).

56. Ganapathy, S. *et al.* Nature of Li2O2 oxidation in a Li-O2 battery revealed by operando X-ray diffraction. *J Am Chem Soc* **136**, 16335–16344 (2014).

57. Gallant, B. M. *et al.* Influence of Li2O2 morphology on oxygen reduction and evolution kinetics in Li-O2 batteries. *Energy Environ Sci* **6**, 2518–2528 (2013).

58. Lu, Y. C. & Shao-Horn, Y. Probing the reaction kinetics of the charge reactions of nonaqueous Li-O2 batteries. *Journal of Physical Chemistry Letters* **4**, 93–99 (2013).

59. Lu, J. *et al.* Aprotic and aqueous Li-O2 batteries. *Chemical Reviews* vol. 114 5611–5640 Preprint at https://doi.org/10.1021/cr400573b (2014).

60. Lim, H. D. *et al.* Rational design of redox mediators for advanced Li-O2 batteries. *Nat Energy* **1**, (2016).

61. Balaish, M., Jung, J. W., Kim, I. D. & Ein-Eli, Y. A Critical Review on Functionalization of Air-Cathodes for Nonaqueous Li–O2 Batteries. *Advanced Functional Materials* vol. 30 Preprint at https://doi.org/10.1002/adfm.201808303 (2020).

62. Xu, W. *et al.* Reaction mechanisms for the limited reversibility of Li-O2 chemistry in organic carbonate electrolytes. *J Power Sources* **196**, 9631–9639 (2011).

63. Gallant, B. M. *et al.* Chemical and morphological changes of Li-O 2 battery electrodes upon cycling. *Journal of Physical Chemistry C* **116**, 20800–20805 (2012).

64. Bryantsev, V. S. & Faglioni, F. Predicting autoxidation stability of ether- and amide-based electrolyte solvents for Li-air batteries. *Journal of Physical Chemistry A* **116**, 7128–7138 (2012).

65. Kwabi, D. G. *et al.* Chemical instability of dimethyl sulfoxide in lithium-air batteries. *Journal of Physical Chemistry Letters* **5**, 2850–2856 (2014).

66. Sharon, D. *et al.* Oxidation of dimethyl sulfoxide solutions by electrochemical reduction of oxygen. *Journal of Physical Chemistry Letters* **4**, 3115–3119 (2013).

67. Schroeder, M. A. *et al.* DMSO-Li2O2 interface in the rechargeable Li-O2 battery cathode: Theoretical and experimental perspectives on stability. *ACS Appl Mater Interfaces* **7**, 11402–11411 (2015).

68. Jiang, Z. & Rappe, A. M. Uncovering the Electrolyte-Dependent Transport Mechanism of LiO2in Lithium-Oxygen Batteries. *J Am Chem Soc* **144**, 22150–22158 (2022).

69. R. D. McLachlan & V. B. Carter. Vibrational spectra of crystalline dimethyl sulfone. *Spectrochim Acta A* **26**, (1970).

70. Zhu, Y. G. *et al.* Proton enhanced dynamic battery chemistry for aprotic lithium-oxygen batteries. *Nat Commun* **8**, (2017).

71. Gao, J. *et al.* Recent progress in hierarchically structured O2-cathodes for Li-O2 batteries. *Chemical Engineering Journal* vol. 352 972–995 Preprint at https://doi.org/10.1016/j.cej.2018.06.014 (2018).

72. Mozhzhukhina, N. *et al.* Insights into dimethyl sulfoxide decomposition in Li-O2 battery: Understanding carbon dioxide evolution. *Electrochem commun* **80**, 16–19 (2017).

73. Ling, C., Zhang, R., Takechi, K. & Mizuno, F. Intrinsic barrier to electrochemically decompose Li2CO3and LiOH. *Journal of Physical Chemistry C* **118**, 26591–26598 (2014).

74. Ferrari, A. C. & Basko, D. M. Raman spectroscopy as a versatile tool for studying the properties of graphene. *Nature Nanotechnology* vol. 8 235–246 Preprint at https://doi.org/10.1038/nnano.2013.46 (2013).

75. Vicentini, R. *et al.* Highly stable nickel-aluminum alloy current collectors and highly defective multi-walled carbon nanotubes active material for neutral aqueous-based electrochemical capacitors. *J Energy Storage* **23**, 116–127 (2019).

76. Nobuyuki Imanishi, Alan C Luntz & Peterr Bruce. *The Lithium Air Battery: Fundamentals*. (Springer, New York, 2014).

77. Dettlaff, A. *et al.* High-performance method of carbon nanotubes modification by microwave plasma for thin composite films preparation. *RSC Adv* **7**, 31940–31949 (2017).

78. Couzi, M., Bruneel, J. L., Talaga, D. & Bokobza, L. A multi wavelength Raman scattering study of defective graphitic carbon materials: The first order Raman spectra revisited. *Carbon N Y* **107**, 388–394 (2016).

79. Lee, A. Y. *et al.* Raman study of D* band in graphene oxide and its correlation with reduction. *Appl Surf Sci* **536**, (2021).

80. Eckmann, A. *et al.* Probing the nature of defects in graphene by Raman spectroscopy. *Nano Lett* **12**, 3925–3930 (2012).

81. Jiang, J. *et al.* A Raman spectroscopy signature for characterizing defective single-layer graphene: Defect-induced I(D)/I(D') intensity ratio by theoretical analysis. *Carbon N Y* **90**, 53–62 (2015).

82. Sengupta, J. & Jacob, C. The effect of Fe and Ni catalysts on the growth of multiwalled carbon nanotubes using chemical vapor deposition. *Journal of Nanoparticle Research* **12**, 457–465 (2010).

83. Yahyazadeh, A. & Khoshandam, B. Carbon nanotube synthesis via the catalytic chemical vapor deposition of methane in the presence of iron, molybdenum, and iron–molybdenum alloy thin layer catalysts. *Results Phys* **7**, 3826–3837 (2017).

84. Schaper, A. K., Hou, H., Greiner, A. & Phillipp, F. The role of iron carbide in multiwalled carbon nanotube growth. *J Catal* **222**, 250–254 (2004).

85. Kim, H. & Sigmund, W. Iron particles in carbon nanotubes. *Carbon N Y* **43**, 1743–1748 (2005).

86. Furlan, A., Jansson, U., Lu, J., Hultman, L. & Magnuson, M. *Structure and Bonding in Amorphous Iron Carbide Thin Films*. *J. Phys.: Condens. Matter* vol. 27 (2015).

87. Wei, T. T. *et al.* Rational construction and decoration of Li5Cr7Ti6O25@C nanofibers as stable lithium storage materials. *Journal of Energy Chemistry* **71**, 400–410 (2022).

88. Yu, G. Q., Tay, B. K., Sun, Z. & Pan, L. K. Properties of fluorinated amorphous diamond like carbon films by PECVD. *Appl Surf Sci* **219**, 228–237 (2003).

89. Tian, Z., Wang, C., Yue, J., Zhang, X. & Ma, L. Effect of a potassium promoter on the Fischer-Tropsch synthesis of light olefins over iron carbide catalysts encapsulated in graphene-like carbon. *Catal Sci Technol* **9**, 2728–2741 (2019).

90. Zhang, Y., Liu, L., Wang, K. & Wang, Y. CTAB-Assisted Synthesis of N-Doped Fe3C Nanowires and Their Magnetic Properties. *J Supercond Nov Magn* **32**, 3503–3508 (2019).

91. Wang, T., Sun, C., Yan, Y. & Li, F. Understanding the active sites of Fe-N-C materials and their properties in the ORR catalysis system. *RSC Adv* **12**, 9543–9549 (2022).

92. Santos, V. P. *et al.* Metal organic framework-mediated synthesis of highly active and stable

Fischer-Tropsch catalysts. *Nat Commun* **6**, (2015).

93. Wei, T. T., Liu, X., Yang, S. J., Wang, P. F. & Yi, T. F. Regulating the electrochemical activity of Fe-Mn-Cu-based layer oxides as cathode materials for high-performance Na-ion battery. *Journal of Energy Chemistry* **80**, 603–613 (2023).

94. He, N. *et al. Growth of Carbon Nanotubules on Fe-Loading Zeolites and Investigation of Catalytic Active Center*. www.elsevier.comrlocatermsec.

95. Peigney, A. *et al.* A study of the formation of single- and double-walled carbon nanotubes by a CVD method. *Journal of Physical Chemistry B* **105**, 9699–9710 (2001).

96. Oliveira, A. A. S. *et al. Magnetic Amphiphilic Composites Based on Carbon Nanotubes and Nanofibers Grown on an Inorganic Matrix: Effect on Water-Oil Interfaces*. *J. Braz. Chem. Soc* vol. 21 (2184).

97. Barros, W. R. P. *et al.* Oxygen reduction to hydrogen peroxide on Fe3O4 nanoparticles supported on Printex carbon and Graphene. *Electrochim Acta* **162**, 263–270 (2015).

98. Zhang, X., Wang, X., Le, L., Ma, A. & Lin, S. Electrochemical growth of octahedral Fe3O4 with high activity and stability toward the oxygen reduction reaction. *J Mater Chem A Mater* **3**, 19273–19276 (2015).

99. Kumar, A., Zhang, Y., Jia, Y., Liu, W. & Sun, X. Redox chemistry of N4-Fe2+ in iron phthalocyanines for oxygen reduction reaction. *Chinese Journal of Catalysis* **42**, 1404–1412 (2021).

100. Ma, Q. *et al.* Stabilizing Fe–N–C Catalysts as Model for Oxygen Reduction Reaction. *Advanced Science* vol. 8 Preprint at https://doi.org/10.1002/advs.202102209 (2021).

101. Sun, X. *et al.* Fluorine-Doped Carbon Blacks: Highly Efficient Metal-Free Electrocatalysts for Oxygen Reduction Reaction. *ACS Catal* **3**, 1726–1729 (2013).

102. Ge, X. *et al.* Oxygen Reduction in Alkaline Media: From Mechanisms to Recent Advances of Catalysts. *ACS Catal* **5**, 4643–4667 (2015).

103. Parthiban, V., Bhuvaneshwari, B., Karthikeyan, J., Murugan, P. & Sahu, A. K. Fluorine-enriched mesoporous carbon as efficient oxygen reduction catalyst: understanding the defects in porous matrix and fuel cell applications. *Nanoscale Adv* **1**, 4926–4937 (2019).

104. Anchieta, C. G. *et al.* LiOH Decomposition by NiO/ZrO2 in Li-Air Battery: Chemical Imaging with Operando Synchrotron Diffraction and Correlative Neutron/X-Ray Computed-Tomography Analysis. *Small Methods* (2024) doi:10.1002/smtd.202301749.

105. Soliman, A. B. *et al.* Tailoring the Oxygen Reduction Activity of Hemoglobin through Immobilization within Microporous Organic Polymer-Graphene Composite. *ACS Appl Mater Interfaces* **9**, 27918–27926 (2017).

106. Fuentes, R. E., Colón-Mercado, H. R. & Fox, E. B. Electrochemical evaluation of carbon nanotubes and carbon black for the cathode of Li-air batteries. *J Power Sources* **255**, 219–222 (2014).

107. Lim, H., Yilmaz, E. & Byon, H. R. Real-time XRD studies of Li-O 2 electrochemical reaction in nonaqueous lithium-oxygen battery. *Journal of Physical Chemistry Letters* **3**, 3210–3215 (2012).